Design of a Semiconductor-Based Proton Spectrometer for Laser-Driven Sources Applications

Francesco Gatti, Francesco Mirani, Dario Rastelli, Davide Mazzucconi, José Luis Henares, Antonia Morabito, Andrea Pola, and Matteo Passoni

***Abstract*— Laser-driven proton sources are attracting increasing interest because of their promising uses in several fields, from basic science to materials analysis. Applications require quantitative and accurate measurements of the laser-driven particle spectra. However, the peculiar features of these sources pose several challenges to their in-depth characterization. In this work, we present the design of a spectrometer based on silicon photodiodes, focusing on TW-class laser proton sources and their foreseen applications. The device comprises a dipole magnet to deflect the ions along different trajectories according to their energies. The magnet can also be removed to avoid beam deflection and make the particles available for applications. We exploit a finely shaped differential filter to cut the contribution of unwanted heavy ions and a photodiode array for proton detection. These elements are described and experimentally characterized, allowing the development of an analytical description useful to size the instrument. We perform Monte Carlo simulations to validate the model and calibrate the system. The retrieved data are used to simulate the detection of protons in a typical laser-driven particle acceleration experiment. The spectrum reconstructed by Monte Carlo simulations well-matches the distribution provided as the source, demonstrating the founding principles of the spectrometer. Finally, a first test in a real laser environment at Centro de Láseres Pulsados (1 PW VEGA-3 laser) is also presented, showing the full response of the device and its potential as a laser-driven proton beam monitor in application-oriented scenarios.**

***Index Terms*— Laser-driven acceleration, laser environment, magnetic spectrometer, photodiodes, proton spectrometry, target normal sheath acceleration (TNSA).**

I. Introduction

SINCE the invention of lasers, thousands of applications have been developed, and thanks to the introduction of the chirped pulsed amplification (CPA) [1], new intensity regimes were achieved. Laser interaction with matter at intensities greater than 10^{18} W/cm^2 allows the generation of various radiation fields, with potential use in a broad range of applications [2], for example, in materials science [3], [4], [5], [6], [7] and radioisotopes production [8], [9].

Laser-driven ion acceleration usually relies on adopting micrometric-thick foils as interaction targets in the so-called target normal sheath acceleration (TNSA) scheme [10], [11]. Highly energetic electrons are produced at the front surface and cross the foil, leaving the target from the rear side. Consequently, an electric field sets due to spatial charge separation (MV/μm), which drives the acceleration of ions present in the contaminants (mainly H and C) up to several millivolt energies. The adoption of engineered targets was also proposed to enhance laser–plasma coupling and, in turn, increase proton energy [12], [13], [14].

TNSA species have unique properties. Protons are emitted in ultrashort pulses in a laminar cone with $\sim$20° aperture and a broad exponential energy spectrum up to tens of millivolts. In the laser-driven environment, both neutral (e.g., X- and γ-rays) and charged species (e.g., C-ions) are present, constituting a complex mixed field. Moreover, during laser–target interaction, other radiations such as intense electromagnetic pulses (EMPs) are generated [15], [16].

These features make the development of adequate instrumentation devoted to particle characterization quite challenging, though essential for the progress of laser-driven acceleration. For example, mixed radiation fields require discrimination strategies for the different species, and EMPs can be an issue for electronic components, causing potential damages and fluctuations in the recorded signals. Indeed, the lack of suitable diagnostics for the different needs in laser-driven experiments has slowed down their deployment in applications.

The development of specialized instrumentation is crucial to unraveling the underlying physics and optimizing the performance of laser-driven proton sources. The ideal diagnostic system should provide single-shot information, measurement of the energy spectrum, angular distribution of the bunch, and discrimination among all other radiation contributions with low sensitivity to electromagnetic noise and good radiation hardness. It must be compatible with vacuum operation and provide the output in real time, thus having a fast response.

Received 4 April 2024; revised 29 July 2024; accepted 7 August 2024. Date of publication 4 October 2024; date of current version 18 October 2024. This work was supported in part by the European Research Council (ERC) through the European Union's Horizon 2022 Research and Innovation Program (PoC-PANTANI) under Agreement 101069171. The Associate Editor coordinating the review process was Dr. Weihua Li. *(Corresponding author: Francesco Mirani.)*

Francesco Gatti, Francesco Mirani, Davide Mazzucconi, Andrea Pola, and Matteo Passoni are with the Department of Energy, Politecnico di Milano, 20156 Milan, Italy (e-mail: francesco.mirani@polimi.it).

Dario Rastelli is with the Raylab s.r.l., 24043 Bergamo, Italy.

José Luis Henares and Antonia Morabito are with Centro de Láseres Pulsados (CLPU), 37185 Salamanca, Spain.

Digital Object Identifier 10.1109/TIM.2024.3472852

A single instrument fulfilling all these requirements does not exist. Thus, in laser-driven ion acceleration experiments, a combination of various techniques, providing complementary information, is adopted. Typically, the same quantities are also measured with different diagnostics to cross-check the results. The detection strategies most commonly adopted, each with its features and limits, include radiochromic films (RCFs) and track detectors (e.g., CR-39), time-of-flight (TOF), and Thomson parabola spectrometers (TPSs) [17], [18].

RCFs [19], [20] are thin sheets of material containing a dye that changes color when exposed to ionizing radiation. By scanning the exposed films, the optical density is measured and directly linked to the (local) absorbed dose. RCF is a passive solution that, used in a stacked configuration, allows reconstruction of the energy spectra of particles, the angular distribution, and the total dose. However, their single-use nature and relatively long processing time, along with their inability to discriminate different radiations, make them unsuitable for real-time characterization of proton beams at high repetition rate operation needed for practical applications.

TOF detectors determine the particle energy based on their flight time over a known distance. Semiconductor detectors are typically employed, such as SiC and diamond. Accounting for the photon signal as a reference, this technique can generally give a quick evaluation of the cut-off energy of accelerated protons, provided that the employed detector has a fast enough response and is placed adequately far from the source. A filter is employed to remove unwanted contributions (electrons and heavy ions) and cut the signal from low-energy protons [21]. Generally, a complex deconvolution procedure [22] is needed to obtain the proton spectrum. The instrument must be calibrated [21], [23] to get quantitative results, and long proton–flight distances are required to get good resolution.

In Thomson parabolas, instead, the combination of magnetic and electric fields, parallel to each other, allows the discrimination of different ion species by imaging the deflected particles on a plane. The magnetic deflection enables the spatial dispersion of the particles, according to their energy. At the same time, the electric field makes the species discrimination possible. In fact, on the detection plane, the ions describe parabolic curves, each related to a specific charge-to-mass ratio, while the position along the tracks accounts for the energy of the particle. Commonly employed sensors are microchannel plates (MCPs) whose converted signal is captured by a CCD camera in real time [24], [25]. However, their absolute calibration is not straightforward since the response can be nonlinear and requires either a conventional accelerator or a cross-calibration, for example, with CR-39 [26]. The high voltage required for the TPS and the MCP demands high vacuum operation ($<10^{-6}$ mbar) to avoid breakdown, posing some constraints when working with gas or liquid targets. Moreover, the instability of voltage supply over time, also due to harsh electromagnetic environments, can affect the resolution of the spectrometer.

In this context, we present a novel proton spectrometer that partially fulfills the mentioned requirements, posing as an alternative to some of the described diagnostics. In our scheme, a magnetic field, generated by a dipole magnet, deviates charged species according to their energy, charge, and mass. Then, heavy ions are removed before reaching the detecting elements, thanks to a filter, produced with the magnetron sputtering technique [27], [28], which is modulated in thickness according to the ions range in matter. Protons are detected with real-time response, thanks to the implementation of a semiconductor-based pixel detector with dedicated front-end electronics, aiming to provide a versatile and reliable tool for the characterization of the whole spectrum of laser-driven protons with absolute calibration. It is interesting to note that just a couple of examples of silicon-based detectors used in laser-driven ion diagnostics are presented in [29] and [30].

This proton spectrometer removes the need for high voltages, though retains the capability of discriminating C-ions. In this way, the issues related to electric field fluctuations during measurements are avoided, and the constraints on high vacuum demand can be relaxed. Quantitative data can be obtained in real time, with the possibility of automated spectrum reconstruction. The setup can be relatively compact with respect to TOF spectrometers, and deconvolution processes for data analysis are not needed. In addition, the device allows for either the measurement or the delivery of the particle bunch for each shot, which can pass through the instrument and be available for irradiation use, also at a high repetition rate.

The working principle and general scheme of the spectrometer are presented, describing all the main components, and their experimental characterization. Its modeling is discussed, and Monte Carlo simulations are used to validate the modeling, refine the calibration, and show the capabilities of the instrument. Test measurements performed during an experimental campaign at Centro de Láseres Pulsados (CLPU, Salamanca, Spain) to assess the response of the device in a real laser environment are presented. This spectrometer proves to be a novel effective tool for laser-driven proton measurement at a high repetition rate in application-oriented scenarios.

II. Operating Principle and Components

The proposed proton spectrometer, schematically depicted in Fig. 1, is based on the principles of magnetic spectrometry, incorporating a dipole magnet and a shaped filter to absorb heavy ions selectively. A pinhole at the entrance assures the selection of a small solid angle, avoiding the uncertainty in the dispersion due to the broad angular divergence typical of laser-driven protons. The primary sensing element is a 1-D photodiode array, providing a robust and efficient means of detecting and quantifying proton signals. Each pixel acts as an individual silicon diode with its separate front-end electronics, independently sized to account for the peculiar exponential shape of the laser-driven spectrum. In this way, high sensitivity can be reached, avoiding saturation issues. Indeed, TNSA features a high number of low-energy particles, each depositing a small amount of energy, and a low number of high-energy particles, also depositing little energy in the detector, with an intermediate region for which the deposited energy reaches a maximum.

The removal of the electric field in the particle deflection stage represents an exceptional simplification compared with

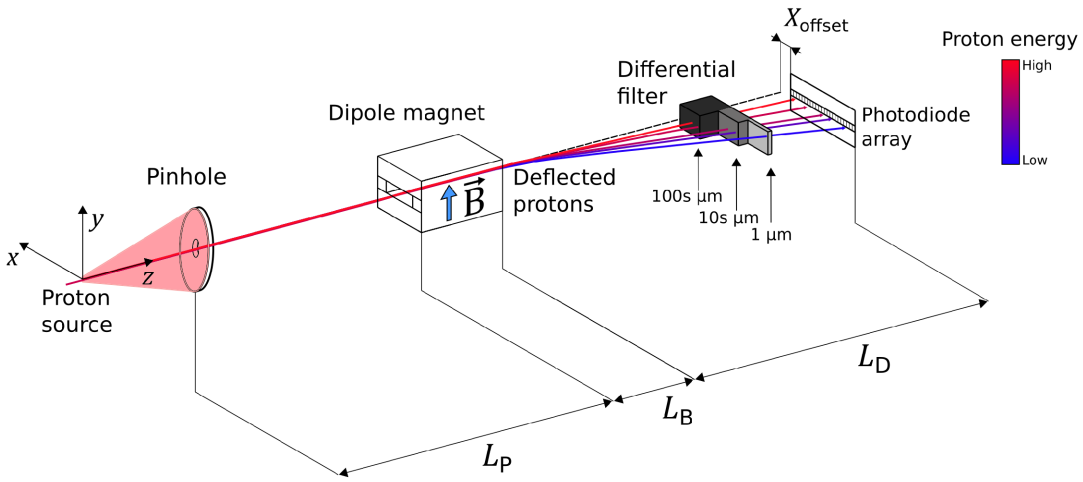

Fig. 1. General scheme of the spectrometer. The main components are shown: pinhole, magnet, heavy-ion filter, and detector. The divergence of the proton point source is represented as a red cone, and the particles selected by the pinhole and deflected by the magnet are depicted as lines colored according to the qualitative colorbar on the right. A pictorial representation of the differential filter shows three different thickness regions. L_p is the pinhole–magnet distance, L_B is the magnet length, L_D is the magnet–array distance, and x_{offset} is the array distance from the axis of the system along the x-direction.

the TPS scheme. It allows for greater flexibility in the experimental setup, avoiding issues related to the risk of electrical breakdown in a vacuum. The energy selection is still defined by the magnetic field, but the discrimination of protons from other heavy ions (mainly carbon ions) is actuated through a metallic filter. This filter has a modulated thickness, which is larger for the higher-energy particles and gets thinner for the low-energy ones, according to their different range in the material. Due to the dependence of the stopping power on the square of the atomic number, carbon ions are stopped by the filter, while protons cross the material and interact with the detector.

In this work, we consider as a reference 100s TW class lasers, thus focusing on the proton energy interval from 300 keV to about 15 MeV [23], [31]. The main elements of the spectrometer are described in detail, and their experimental characterization is discussed in the following.

A. Permanent Dipole Magnet

The sizing of the magnet is the first step in the design of the spectrometer since it determines the required positioning of the successive elements (i.e., the differential filter and the photodiodes).

The magnet has a maximum field of 0.4 T over 50-mm-long plates. The gap between them is 10 mm, and the lateral aperture is 37 mm. The measured magnetic field is uniform inside the plates (1% deviation), but the fringes that extend outside must be considered. For this reason, a field map was recorded on a 19 × 5 × 123 grid employing an FW Bell 5170 Gauss meter. The accuracy of the instrument is ±1% (according to the manufacturer's specification). The result is shown in Fig. 2(a), while in Fig. 2(b) can be seen the detail of the field intensity profile in the yz plane for $x = 0$. Modeling a nonuniform and spatially limited magnetic field with a unique average value can introduce nonnegligible errors in the evaluation of proton deflection at different energies. For this reason, we evaluated an effective magnetic field function of the proton energy $B_{\text{eff}}(E)$. In this way, the uncertainty in the particle deflection evaluation is minimized. For instance, in the energy range 0.3–30 MeV, B_{eff} varies from 542 to 528 mT. Note that an error up to several mm in low-energy proton position at photodiodes location is made if an average value is considered. For these reasons, we adopted $B_{\text{eff}}(E)$ in the analytical model. Monte Carlo simulations are instead possible to directly include the full field map.

B. Differential Filter

The dependence of the stopping power of materials with particle charge is quadratic. Thus, this behavior can be exploited to selectively separate the species of a mixed field like the TNSA one, introducing a differential filter. C-ions are accelerated together with H^+. It must be highlighted that, although C^{6+} have the shortest range among all the charge states, they also have the highest charge-to-mass ratio and, therefore, they are accelerated to the highest energies by the sheath field [32]. For this reason, they are considered representative carbon ions in the calculations. The ranges in Cu as a function of ion energy for both C^{6+} and H^+ are reported in Fig. 3(a) as retrieved from SRIM [33].

The material thickness needed to stop the heavy ions is a function of the particle energy. A simple foil absorbing high-energy ions would also cut the low-energy protons (hundreds of keVtofew MeV). These protons represent the highest number of particles due to the exponential shape of the spectrum. Since we want to characterize also this region quantitatively, in particular, in view of applications, a spatially modulated thickness profile considering the magnetic dispersion of the particle is needed. In the system calibration (described below), the energy loss of protons inside the filter must be accounted for in the evaluation of the mean charge deposited by a single proton event in each pixel.

An example of a filter profile is reported in Fig. 3(b). It is computed considering a combination of Cu and Al layers. This choice comes from considerations about the production

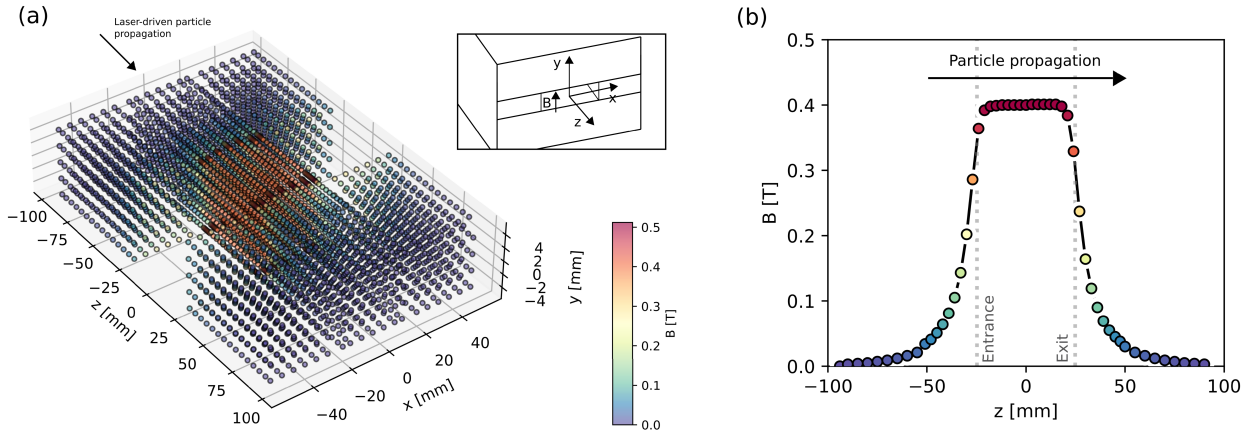

Fig. 2. Measured magnetic field with the adopted reference frame, in particular (a) complete 3-D field map and (b) field profile along z at $x = 0$ and $y = 0$.

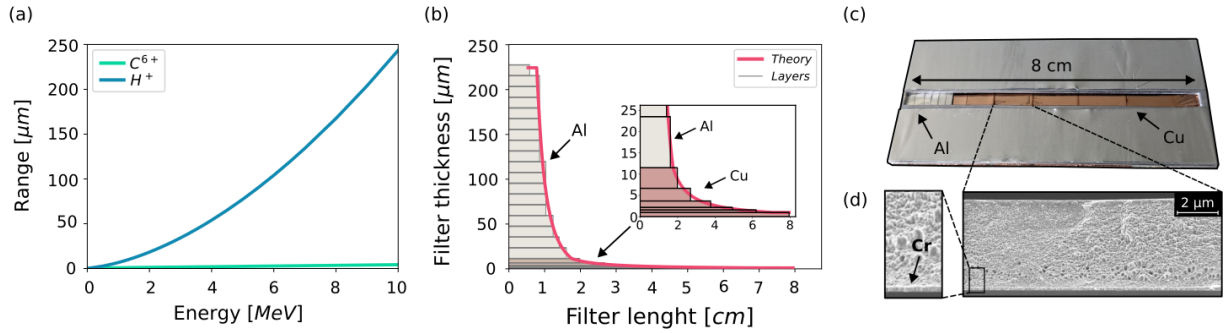

Fig. 3. (a) Continuous slowing down approximation (CSDA) range in matter from SRIM for protons and fully ionized carbon ions in copper in the range 0–10 MeV. (b) Theoretical filter profile and optimized layered reconstruction for the investigated spectrometer configuration. (c) Picture of the produced filter. (d) SEM images of a representative layer in which the Cu and Cr regions are visible.

procedure, detailed in the next paragraph. Reproducing the exact theoretically calculated profile is not practical (a continuous variation of the thickness on the microscale is challenging to achieve). Thus, we developed an algorithm that computes the best approximation of such a profile in a layer-by-layer fashion, giving as input the adopted materials and the number of layers or the available foil thicknesses. The thickness in each position must be equal, at least, to the range in the material of the carbon ions hitting the filter. Nevertheless, we accounted for a "safety factor," thickening the filter to compensate for possible misalignment, based on a maximum foreseen error (e.g., 1 mm).

Proton scattering inside the filter can reduce the number of particles interacting with the pixels. To minimize this effect, the filter must be placed as close as possible to the photodiode array. The filter can be put on support together with the array so that its relative position is kept fixed. In addition, the filter provides added shielding against X-rays, EMPs, and possible scattered light.

Regarding the production of the filter, we used the magnetron sputtering [34], [35] system present in our laboratory at Politecnico di Milano, to grow it layer-by-layer. This technique allows the deposition of thin films with good uniformity over large areas with near-bulk densities and optimal control of the thickness. Magnetron sputtering is suitable for film thicknesses up to a few μm. Therefore, we considered materials with relatively high densities and atomic numbers to keep the required thicknesses contained. Combining this requirement with the need for a high deposition rate, copper was selected as the best candidate [36]. The first layer of the filter is produced by adopting the same strategy described in [37], depositing the thin film on a silicon wafer covered with a sacrificial layer, enabling its detachment after growth by dissolution in water. Thicknesses down to tens of nm are achievable, though for the first layer production 817 $\pm$ 20 nm and 995 $\pm$ 16 nm thick films were deposited. The thickness of the five subsequent Cu layers spans from 700 nm to 5 μm. A few nm chromium interlayer (80 $\pm$ 4 nm) is also deposited between Cu layers to improve adhesion [38], [39]. Its stopping power is accounted for in the required thickness computation. Finally, in the high-energy region of the filter, where the material thickness is too high to be easily deposited by magnetron sputtering, 13 μm Al commercial foils are fixed in position. An example of the final result is presented in Fig. 3(c), while in Fig. 3(d), SEM cross-section images of a Cu and Cr layer are shown. Cross-section images are used as the main tool to measure the thickness of the layers.

C. Photodiode Arrays

The choice of silicon photodiode array as the detecting element is guided by the chance to achieve real-time response,

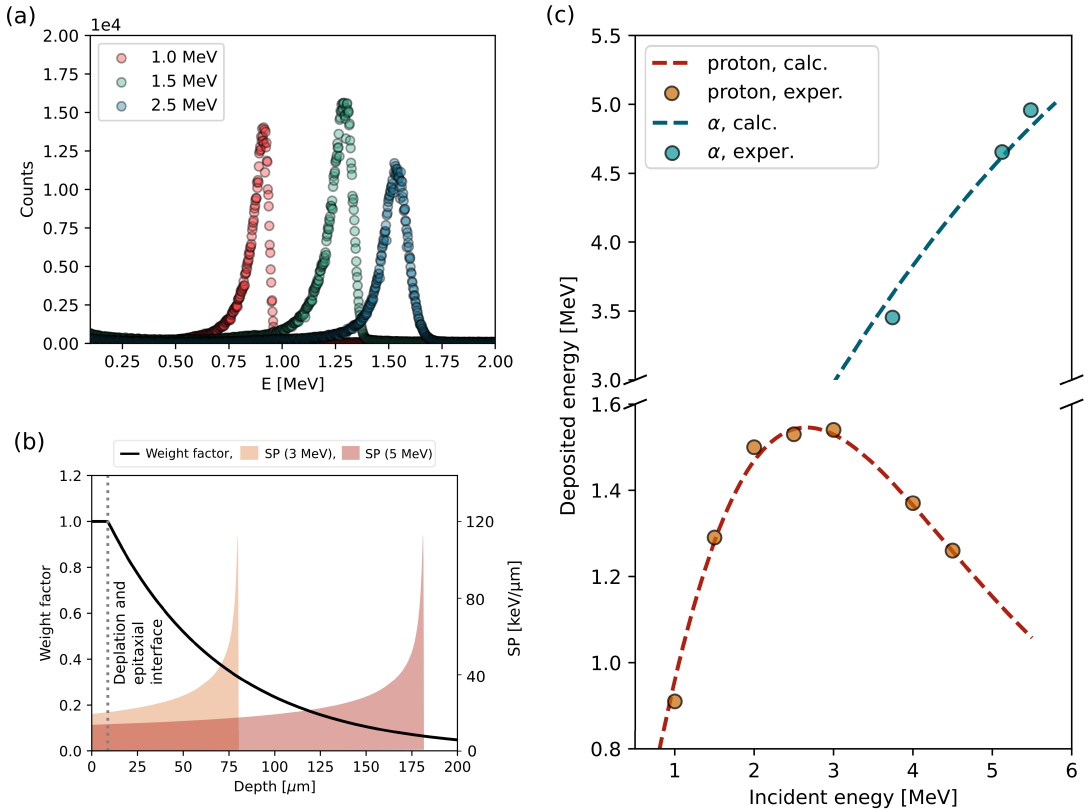

Fig. 4. (a) Calibrated pulse height spectrum under proton irradiation at 1.0, 1.5, and 2.5 MeV. (b) Modeled CCE with full collection in the depleted region and diffusion-driven collection at greater depth; stopping power as a function of depth for 3- and 5-MeV protons is superimposed. (c) Experimental values of deposited energy as a function of different incident energies for protons and alpha particles, and the fit curve corresponding to the modeled CCE.

and the versatility coming from the availability of many different commercial solutions in terms of pixel dimension, number, pitch, and sensitivity. Moreover, they allow for embedded readout and quick data analysis. Photodiode arrays are also easily replaceable when irradiation damage becomes too high, possibly without the need for a complete recharacterization thanks to their good reproducibility.

For the first investigation and modeling of the spectrometer, we consider one of the simplest and cheapest arrays suitable for this application, that is, Osi Optoelectronics' A2V-16. They have 16 pixels with an area of 1.92 mm^2 and 1.59 mm pitch. They can be easily stacked in line to increase the energy range. In particular, we considered a series of three arrays, for a total of 48 pixels. The pixels were characterized in terms of capacitance measurements, as well as response to alpha particles and proton irradiation. The variability of such parameters among different arrays was also investigated.

Capacitance measurements at complete depletion resulted in 23 ± 1 pF, with a relative variation between different arrays of about 2%–4%, corresponding to a depleted region thickness of 8.7 ± 0.4 μm. This value is related to the charge-collecting region of the adopted photodiodes, and thus it is necessary for the absolute calibration of the detector.

We used a ^{241}Am source to study the response to irradiation of particles having the same charge-to-mass ratio as C^{6+}. The experiment was performed in air, in a vacuum, and with a thin Al foil to get different alpha particle energies at the expense of broadening. The incident energies were retrieved with Monte Carlo simulations. In addition, single proton irradiation was performed by exploiting a conventional Van de Graaff accelerator. Proton energy was scanned between 1 and 4.5 MeV. Some pulse height spectra are shown in Fig. 4(a). In these conditions, low cross-talking is observed, also due to the relatively large sensitive areas.

For both investigated species, the calibration resulting from the measured deposited energies cannot be interpreted considering the depleted region thickness retrieved from capacitance measurements. The measured values are compatible with a charge diffusion process in silicon. In fact, in the bulk p-doped zone, the carrier transport is dominated by the diffusion mechanism toward the depletion region, since no electric field is present [40], [41]. If the integration time is longer than the carrier lifetime, this effect has to be considered. Thus, we modeled the charge collection efficiency (CCE) in the form of a constant value of 100% in the first region plus an exponentially decaying CCE [40] as

$$\mathrm{CCE}(z) = \begin{cases} 1, & \text{for } z < a \\ e^{-\frac{(z-a)}{\lambda}}, & \text{for } z > a \end{cases} \tag{1}$$

where z is the depth in the detector, a is the position of the interface between the two regions, and λ is the electron diffusion length. By fitting the proton deposited energy as a function of incident proton energy, we found

$a = 8.8$ μm and $\lambda = 63.1$ μm. a is very close to the depleted region thickness retrieved from the capacitance measurement, while the diffusion length corresponds to a carrier density $N \simeq 6 \times 10^{17}$ cm^{-3}, that is reasonable for a common silicon-based photodiode [42].

The modeled CCE is reported in Fig. 4(b), while the experimental points and the curve obtained from the modeling can be seen in Fig. 4(c). The deposited energy in silicon as a function of the incident proton energy shows a maximum of around 3 MeV. Such behavior is the result of the combined effects of stopping power for different particle energies and the CCE as a function of penetration depth [see Fig. 4(b)]. At low incident proton energy, the number of charge carriers produced in the electric field region or in its proximity, where the diffusion process is relevant, increases by increasing particle energy. Above 2–3 MeV, most of the energy is deposited deep in the silicon, where the CCE is low and charge carriers in the absence of the electric field tend to recombine. The same CCE curve is used to evaluate the energy deposited by alpha particles. In this case, the stopping power is much higher. Thus, for the investigated energy range, we do not observe yet a decrease in the deposited energy. It shows good agreement with the measured values. This modeling is considered in the design of the spectrometer.

D. Front-End Electronics

Direct charged particle detection with semiconductors is based on the conversion of the incident radiation energy to electron–hole pairs in the material. These charge carriers can thus be collected at the electrodes and converted to a suitable (voltage) signal to be read (see inset in Fig. 5). The number of the produced pairs is directly related to the energy deposited in the detector by the incident particle. In the spectrometer presented in this work, the magnetic field selects the energy of the particles impinging on each pixel, thus determining the number of carriers produced by each proton. Rather than the single particle interaction, the quantity of interest is then the number of interacting particles for each pixel, proportional to the total charge carriers produced by the whole proton bunch.

The front-end electronics of the spectrometer are designed to integrate the charge produced by all the impinging protons, keeping in mind the features of TNSA acceleration. Indeed, the exponential spectrum of laser-driven protons poses some challenges, and a wide dynamic range is required to enable the detection of both very large amounts of particles at lower energies and few ones in the proximity of the cutoff.

The basic circuit is composed of a charge-sensitive preamplifier, shown in Fig. 5. The biasing voltage source V_{bias} and its dc-blocking capacitor C_{block}, which prevent dc signals from being transmitted through the circuit while allowing ac signals to pass through, are also pictured. By implementing appropriate feedback capacitors C_{feed} and resistors R_{feed} for each pixel, the correct modulation of the detection range can be achieved. In particular, C_{feed} is sized according to the expected amplitude of the current pulse generated in the photodiodes, while R_{feed} is chosen to match a suitable time constant for the circuit compatibly with the noise level.

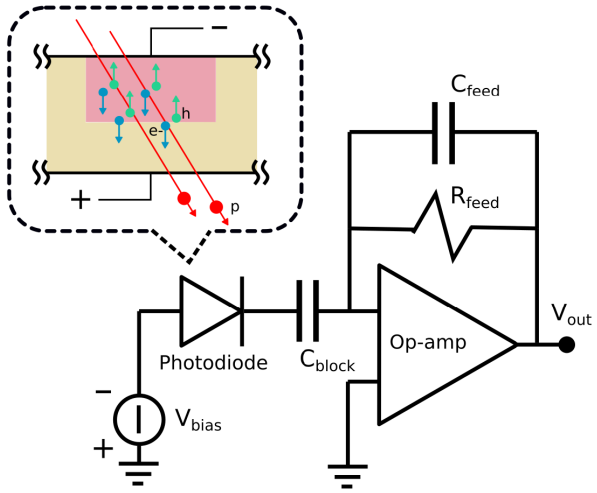

Fig. 5. Basic circuit scheme of the front-end electronics of each pixel. The bias voltage source V_{bias}, the needed blocking capacitor C_{block}, the photodiode, and the preamplifier, that is, op-amp with C_{feed} and R_{feed}, are shown. The inset reports a schematic of protons (p) impinging on the photodiode and the generation of electron (e−)–hole (h) pairs.

The sizing of the capacitor is based on the expected proton spectra in a certain condition, that is, a specific class of lasers (10s TW, 100s TW, PW) considering the TNSA scheme, choosing a desired output voltage V_{out} as reference (e.g., 1 V). However, signals from a few millivolts to a few volts can be managed for each pixel, allowing almost three orders of magnitude range of detection, since they scale linearly with the number of protons. In addition, the adopted setup allows tuning the solid angle seen by the diagnostic by modifying the distance from the source and/or the pinhole diameter, increasing or reducing the protons interacting with the spectrometer.

III. Spectrometer Modeling and Simulations

The presented spectrometer is modeled analytically to retrieve basic information such as mean energies and energy bin width, along with the mean charge generated per incident proton in each pixel (i.e., calibration). These data are used to size the spectrometer in terms of the position of the photodiode array relative to the magnet.

Starting from the design obtained from the model, the same system is implemented in a Geant4 [43] Monte Carlo simulation, introducing also the optimized layered filter. A more reliable calibration of the device is thus achieved and it is used to test its spectral reconstruction capabilities. The differential filter effectiveness is also investigated with a dedicated set of simulations.

A. Analytical Model

In a magnetic spectrometer, protons describe a straight line on a screen put after the magnet. The position on this line is directly linked to the particle energy. The equation that relates energy and position is the same describing the deflection of particles along the magnetic axis in Thomson parabolas. In particular, considering a uniform magnetic field B with

length L_B and a propagation distance L_D, as also depicted in Fig. 1, we have

$$X(E_k|q,m) = \frac{qB}{\sqrt{2mE_k}} - \sqrt{\frac{2mE_k}{(qB)^2} - L_B^2} + \frac{L_B L_D}{\sqrt{\frac{2mE_k}{(qB)^2} - L_B^2}} = R - \sqrt{R^2 - L_B^2} + \frac{L_B L_D}{\sqrt{R^2 - L_B^2}} \quad (2)$$

where q, m, and E_k are the particle charge, mass, and kinetic energy, respectively. The Larmor radius R is also introduced. It is worth noting that often it is considered that $R \ll L_B$, and thus the equation simplifies to $(L_B L_D)/R$ [44], [45]. If different ion species are present, particles with the same energy will end up at different points due to the $q/\sqrt{m}$ dependence. Given a specific magnetic field strength and length, decreasing the distance L_D will result in lower deflections and lower resolution for the spectrometer.

Equation (2) can be numerically inverted to find the kinetic energy of protons as a function of the position on the detector $E_p(X)$. It is a monotonically decreasing function, reflecting that particles with higher energies suffer lower deflections from the field and can be exploited to model the spectrometer. In fact, the proton energy associated with each pixel, $\bar{E}(N)$, and its bin width, $\Delta E(N)$, can be calculated as

$$\bar{E}(N) = -\frac{1}{x_p}\int_{Nx_p}^{(N-1)x_p} E_p(X)dX \quad (3)$$

$$\Delta E(N) = E_p\big(Nx_p\big) - E_p\big((N+1)x_p\big) \quad (4)$$

with x_p being the pixels width along x, and N the pixel enumeration, and $N = 1, 2, 3, \ldots, N_{\text{px}}$ (with N_{px} maximum number of pixel, i.e., 48).

The trend of E_p makes the energy bin larger as the energy increases, thus worsening the energy resolution of the system. Nevertheless, the growth of the energy bin is beneficial in the case of laser-driven proton exponential spectra. Indeed, the low-energy part of the spectrum, consisting of many protons that release a high amount of energy, is distributed over many pixels, reducing the possibility of saturation. Conversely, the high-energy part, consisting of a few protons that release a small amount of energy, is compressed in some pixels, increasing the low signal generated by such protons. The dimensions of the photodiodes play a major role since smaller pixels allow for better resolution or more compact devices at the expense of complexity.

The deposited energy in the detector can be computed using SRIM tables for the stopping power of protons in silicon. By dividing such a value by the energy required to produce an electron–hole pair $\epsilon_{\text{Si}} \simeq 3.62$ eV, the mean generated charge per incident proton can be computed. Note that the calculation needs to be adjusted considering the modeled CCE for the adopted photodiodes. The mean charge generated in the detector per incident proton for each pixel, $\bar{Q}(N)$, can be calculated with the same approach adopted for $\bar{E}$

$$\bar{Q}(N) = -\frac{1}{x_p}\int_{Nx_p}^{(N-1)x_p} Q_{\text{px}}(X)dX \quad (5)$$

TABLE I
SUMMARY OF THE PARAMETERS EMPLOYED IN THE SPECTROMETER MODELING

B	L_B	x_p	L_D	N_{px}	X_{offset}
$B_{eff}(E)$	5 cm	1.22 mm	23.5 cm	16x3=48	5 mm

where $Q_{\text{px}}(X)$ is the locally deposited charge as a function of the position on the detector.

$\bar{Q}(N)$ is the core of the quantitative calibration of the spectrometer. In measurements, the maximum output voltage from the preamplifier V_{out} is converted to the corresponding charge $Q_{\text{out}}(N) = C_f(N) \cdot V_{\text{out}}(N)$, with C_f being the feedback capacity of the circuit. Finally, the number of incident particles for each pixel is retrieved as $N_p(N) = Q_{\text{out}}(N)/\bar{Q}(N)$. A more accurate estimate of $\bar{Q}(N)$ can be obtained from Monte Carlo simulations, described in Section III-B, also accounting for other possible radiations interacting with the sensors.

This model is implemented considering the described components (i.e., magnet and photodiode arrays). The employed parameters are summarized in Table I. L_B, B, and x_p are fixed, L_D the free parameter for the sizing of the spectrometers, N_{px} the number of pixels (equal to an integer multiple of 16, the number of pixels per array), and X_{offset} the offset from the beam axis (see Fig. 1). Note that, as explained in Section II-A, we use the function $B(E)$ for the magnetic field intensity rather than a single value.

Since we would like to let the particle pass through the instrument by removing the magnet without altering the alignment, we can set a lower bound to the value of X_{offset}. We put it equal to 5 mm. Other constraints can be added as the minimum and/or maximum detectable energy and the maximum acceptable bin width at a fixed energy. We considered investigating an energy range of about 0.3–10.0 MeV and a maximum bin width at 10.0 MeV of about 1.5 MeV (i.e., $\sigma = \pm 7.5\%$). This approach allows us to retrieve an optimal configuration in terms of L_D. In fact, X_{offset} can be fixed to its lower bound, and the number of arrays is linked to the deflection of the lowest detectable energy. We found that the minimum number of arrays needed to satisfy the constraint on the bin width is 3. Evidently, this implies that some pixels at higher mean energy are present, though with quite poor resolution.

Fig. 6(a) shows the scheme of the three arrays configuration, associating a color to each of them and the main results of this model are shown in Fig. 6(b) and (c). The mean proton energy associated with each pixel in Fig. 6(b) is an increasing function since pixel enumeration corresponds to the deflection axis. In fact, its shape is directly linked to E_p. The last two pixels are excluded in the plot for clarity since they correspond to very high energies with extremely poor resolution (i.e., 72 ± 15 MeV). As anticipated, the energy bin width increases while decreasing the deflection. It is reported as a function of mean proton energy in Fig. 6(c). The uncertainty associated with each channel can be considered as $\pm$half the bin width, giving the main contribution to the energy resolution of the spectrometer, which ranges from 3% to 26%. The mean charge produced in the photodiodes by a single impinging proton as

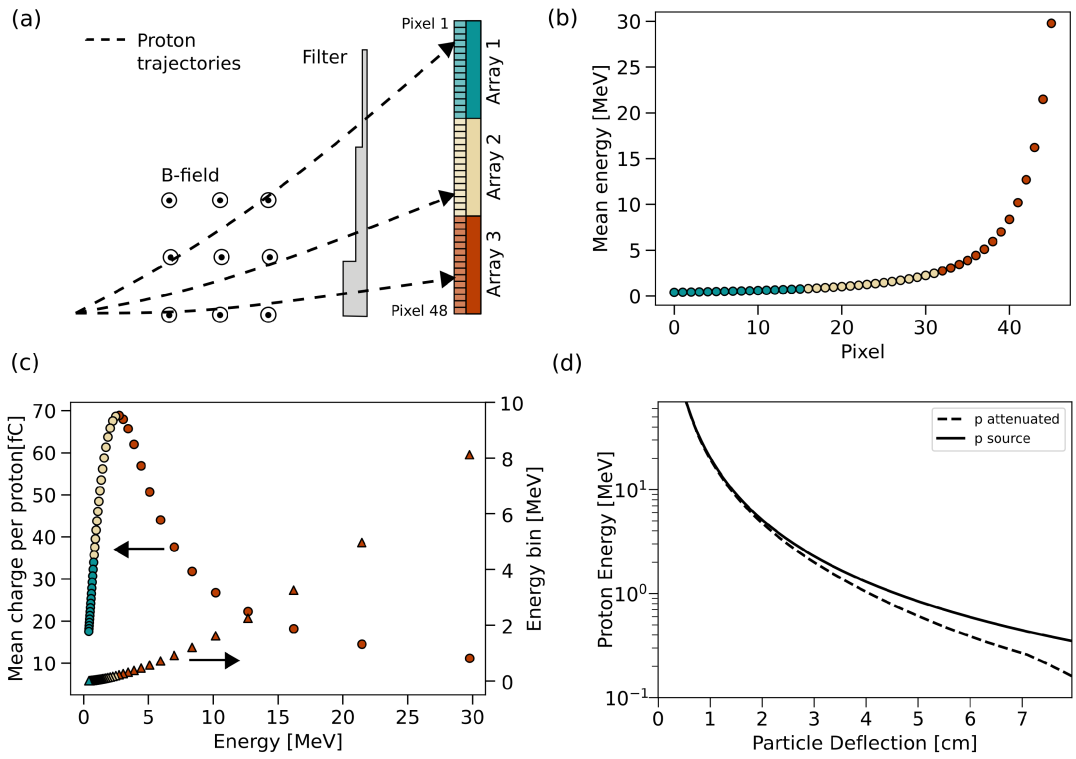

Fig. 6. (a) Schematic representation of the three arrays setup. (b) Computed mean proton energy associated with each pixel. The last two pixels (44 and 72 MeV) are omitted for clarity. The three colors identify the three different arrays of photodiodes. (c) Full energy bins as a function of proton mean energy and the mean charge produced in the photodiodes by a single impinging proton as a function of proton mean energy. (d) Proton energy as a function of the spatial position along the deflection axis with (solid line) and without (dashed line) the differential filter on the detector plane. The vertical difference between the two lines corresponds to the energy loss.

a function of proton mean energy is reported in Fig. 6(c). The peaked shape of this function is mainly due to the stopping power of silicon as a function of energy, deformed by the effect of the CCE trend. In fact, with respect to a sharp depletion region condition, the relevant energy deposition region is extended for middle-to-high energy particles. A charge of a few tens of fC per particle is generated in each pixel.

Here, we did not consider the presence of the filter, which makes the impinging protons less energetic and thus modifies the calibration, with an overall effect on $\bar{Q}(N)$. Moreover, scattering events occur, with a possible variation of mean energy and energy bin width. The first effect can be considered by computing the energy loss in the material, building a transfer function from the incoming spectrum to the one spatially dispersed after the differential filter. Fig. 6(d) shows this function. The filter is placed 2 cm in front of the detector. The calibration is adjusted using this corrected E_p trend.

The introduction of proton scattering and secondary radiation generation in the analytical model is not so straightforward. We thus performed simulations to validate the described result, improve them, and test the spectrum reconstruction in a proton–ion mixed field.

B. Monte Carlo Simulations

To validate the presented model, the detector is implemented in the geometry of a Monte Carlo simulation using the Geant4 toolkit. The magnetic field is imported as the full experimental table represented in Fig. 2(a), and the photodiodes thickness is divided into two regions as depicted in Fig. 4(b). To validate the analytical model, a pencil beam with a uniform energy spectrum ranging from 100 to 50 MeV is considered, shooting 8×10^7 primary protons. The initial energy of all the impinging protons is recorded for each pixel. In addition, the entire deposited energy in the first region and the exponentially corrected one for the diffusion part is retrieved, allowing us to compute the mean produced charge per impinging particle.

The mean charge per proton obtained from the Monte Carlo simulation is shown in Fig. 7(a), also in comparison with the analytical result retrieved in Section III-A. Such quantity is particularly relevant since it is the core of the absolute calibration of the instrument. There is good accordance between the trend evaluated with the Monte Carlo and the analytical one. In particular, at energies greater than about 2 MeV, the difference between the two is always less than 5%. In fact, the energy loss in the filter and the deviation from their straight path are relatively low. That is not the case for lower-energy particles, for which these effects become relevant. Indeed, in this region, the relative difference with the model is higher, increasing up to 40% below 600 keV. Here, the energy deposited per particle decreases, due to the energy loss in the filter. On the other hand, the energy deposition for higher energy pixels slightly increases, as expected, due to the slightly higher stopping power. Considering average energy and bin

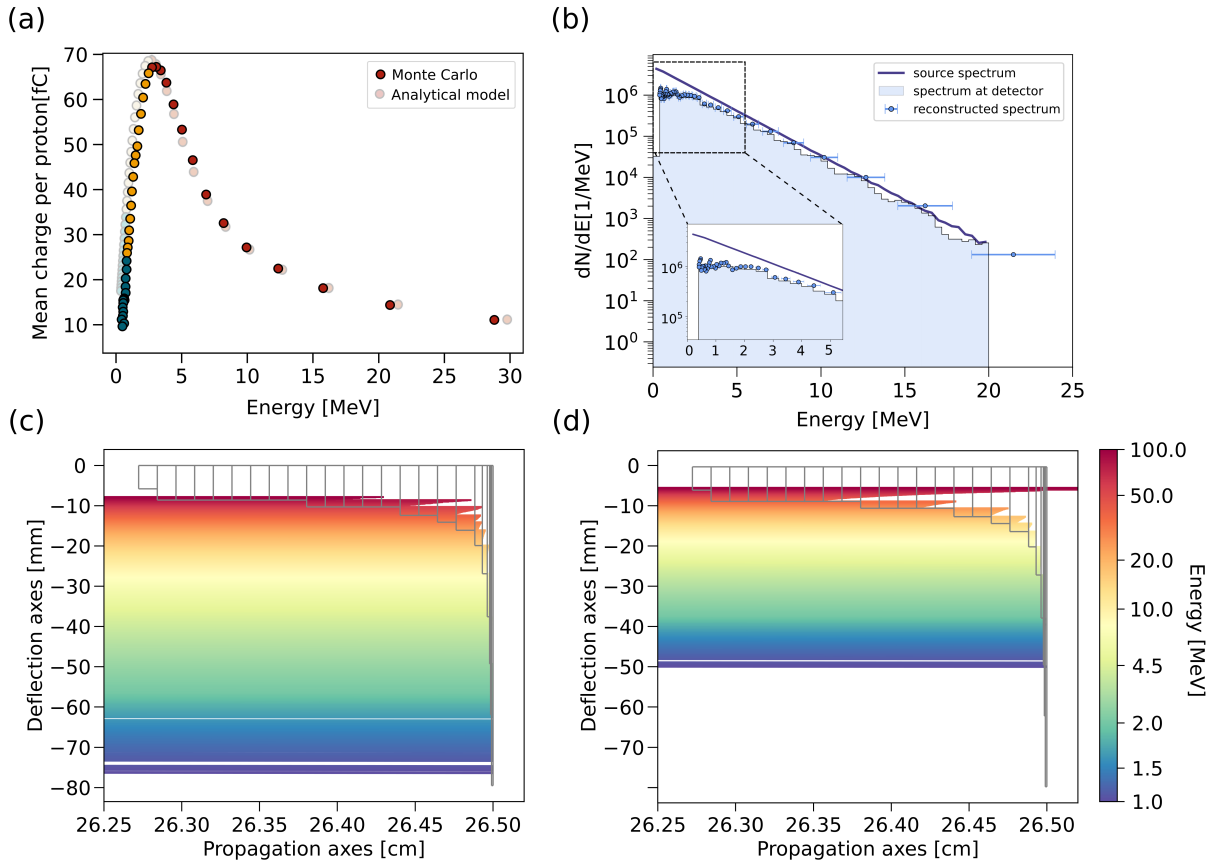

Fig. 7. (a) Mean deposited charge as a function of average pixel energy as computed from Geant4 Monte Carlo simulations. The light points represent the analytical model results. (b) Exponential proton spectrum was reconstructed with the described approach and setup (points with error bars). The spectrum at the source (solid line) and the detector plane (light-blue area) are plotted for comparison. (c) C^{6+} and (d) C^{4+} trajectories for different energies and interaction with the differential filter.

width for each pixel, no significant deviations are observed since the contribution of scattered particles is generally low.

The retrieved calibration is employed to reconstruct the incident spectrum from an exponential proton source (maximum energy $E_{\max} = 20$ MeV and temperature $T = 2$ MeV) that should mimic a laser-driven one. Again, 8×10^7 primary protons are simulated. Fig. 7(b) shows the spectra at the source (purple solid line) and the reconstructed one (points with error bars). Since some particles are lost and not detected due to the step-like shape of the filter and proton scattering, the agreement is partial at low proton energies [see the inset in Fig. 7(b)]. On the other hand, the reconstructed spectrum and that associated with protons incident on the arrays (filled histogram) well coincide at all energies. Therefore, a transport efficiency considering scattering events for the specific geometry can be introduced. The value of such a correcting factor can be computed from the Monte Carlo simulation as the ratio between the spectrum at the source and the one at the detector plane. Taking into account this efficiency, we can obtain the spectrum at the source without the underestimation at low energies.

The effectiveness of the differential filter is investigated by simulating carbon ion irradiation for the same geometry. Fig. 7(c) and (d) shows the trajectory of C^{6+} and C^{4+} ions, respectively, in the energy range 1–100 MeV. The higher charge state particles, considered to size the filter, are completely stopped for all energies. Instead, the C^{4+} ions are stopped up to about 81 MeV, while more energetic ones can pass through the filter. As anticipated, tough, the particles accelerated to the highest energies are the ones with greater charge-to-mass ratio. In addition, the trajectories of such high-energy ions will impinge on the first pixels, excluded due to their poor resolution. A thicker last layer can also be implemented to overcome this issue.

It is worth noting that the filter is designed according to the magnetic field, the detector position, and its characteristics, having in mind the expected energy range of the ions. In experiments for which higher energies are expected, like in the case of PW class lasers, the developed algorithm can be used to properly optimize the required differential filter. The simulations validated the design procedure for the component that can also be applied to different scenarios.

IV. Electronics Response in Laser Environment

Assessing the reliability of the proposed instrument in a real scenario is fundamental. In particular, the behavior in a laser interaction experiment where scattered light, EMPs, and other sources of noise are present, needs to be tested. Thus, during an experimental campaign at Centro de Láseres

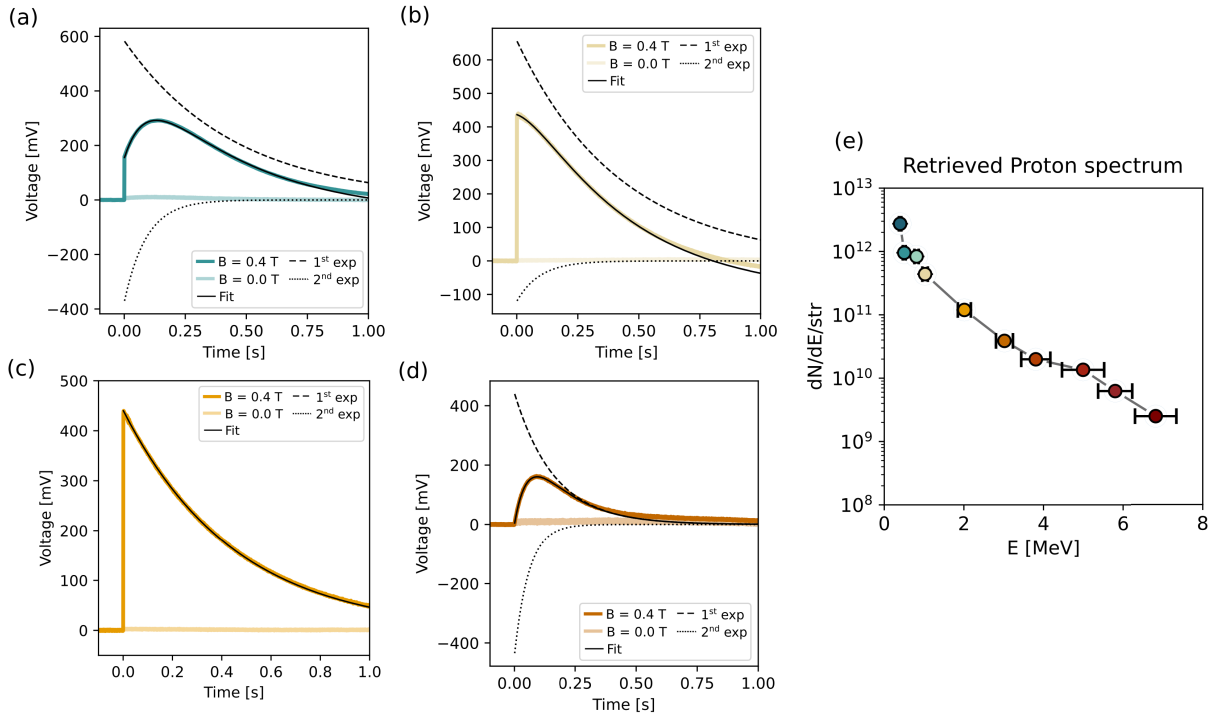

Fig. 8. (a)–(d) Selected voltage pulses recorded in the laser-driven acceleration experiment, representative of the measured signals. Each plot shows a different pixel, with its response with (colored line) and without (gray line) the magnetic field. Each signal is well-fit by a sum of two decaying exponentials with opposite signs (dashed lines labeled as first exp and second exp in legends) with different weights and characteristic time constants due to induced charge and electric field shielding. (e) Example of the reconstructed calibrated spectrum from the measured voltage pulses in logarithmic scale.

Pulsados (CLPU) in Salamanca (Spain), we exploited the 1-PW VEGA-3 laser [46] (∼30-fs time duration, 12-μm FWHM focal spot, $\sim 1 \times 10^{20}$ W/cm^2 peak intensity) to test the spectrometer. Although, as anticipated, this instrument is designed mainly for TW-class lasers in terms of energy range, the PW scenario investigated is a good testing ground, as it provides a more challenging environment in terms of possible noise sources.

To study the instrument response in a real scenario, a selection of pixels distributed on the three arrays, spanning the proton spectrum from 400 to 7 MeV, was investigated. Front-end electronics charge amplifier voltage outputs were recorded on a Picoscope 4824 during the experiment. At the entrance of the instrument, flanged to the interaction chamber, a 1-mm diameter pinhole is used to select the particles. The spectrometer is located along the laser axis, at 12° from the target normal, with a target-to-photodiodes distance of 186 cm. This configuration, combined with the off-axis positioning of the filter and photodiodes by X_{offset}, avoids the possible detrimental effect of debris deposition on the filter.

To investigate the presence of noise and the effect of EMPs, we first removed the dipole magnet, so that no charged particle would interact with the detector. Afterward, the magnet is introduced to use the device as a spectrometer.

The raw signals of the spectrometer are presented in Fig. 8(a)–(d) for different channels. The gray lines represent the signals without the magnetic field, showing that the background perturbation due to the laser shots is negligible compared to the proton signals (colored lines). The acquired pulses are different for the various pixels, and only one shows the expected exponential decay determined by the product of the RC feedback [Fig. 8(c)]. The signal measured on all the other pixels is found to be a superimposition of two different exponential functions, with the resulting shape well-fit if a negative exponential is followed by a positive one (reported in Fig. 8(a), (b), and (d) as dashed lines). This behavior was not observed during the proton irradiation of photodiodes performed with the electrostatic accelerator (see Section II-C) since only single-particle response was investigated. Such shape could be the result of a combination of effects, that is, induction between the different pixels on the same array, that are characterized by a common cathode, and a slower current pulse formation.

In fact, the high density of electron–hole pairs produced in a short time by the incoming protons could be responsible for this effect by introducing partial shielding of the electric field in the depleted region. The effects related to high carrier density tracks produced in semiconductor detectors are referred to as plasma effect [47], [48], which typically determines a delay in the current pulse formation. However, this effect is usually investigated for heavy ions or pulsed-operated detectors. In laser-driven experiments, instead, the "plasma" region is extended to the whole active region, rather than to a column or sphere or electron–hole pairs, making the treatment of charge transport even more difficult. Despite the temporal delay introduced by such an effect, since we integrate the whole current pulse, the relevant information on the deposited charge is preserved. Considering different laser

shots, we also observed that each pixel has always the same temporal evolution, thought, with amplitudes that differ from shot to shot. Since induction effects are related to the charge distribution in space in the whole array, a possible explanation for this behavior is that the relative amount of charge generated in neighboring pixels is quite similar for all the shots. This is ascribable to the intrinsic exponential nature of TNSA proton spectra.

In this condition, accounting also for the induction effect, the value related to the deposited charge to be exploited for retrieving the incident proton spectrum is the one extrapolated from the fit as the amplitude of the positive exponential, which corresponds to the charge that would be collected in absence of the induction effect. Since such an effect produces a zero-average signal, considering the integral in time of the voltage instead of its peak allows for avoiding the exponential fit, giving an alternative solution to speed up the data analysis in future developments.

The temporal waveforms of the recorded signals determine the maximum repetition rate sustainable by the spectrometer. They must return to the baseline level (i.e., about 0 V) before a new proton bunch can be detected. We can estimate $\approx$0.5 Hz as the maximum repetition rate for the specific electronics adopted in this work. In the case of higher repetition rate operation, the feedback electronics can be adjusted by tuning the resistance to reduce the response time constant.

Fig. 8(e) presents the resulting calibrated spectrum per unit solid angle for a single shot. In the logarithmic scale, it can be seen the approximately exponential decrease with energy, as the typical TNSA spectra. The cutoff energy is found at 7.0 ± 0.5 MeV. Considering the adopted laser parameters, this result agrees with experimental data reported in literature [49]. The same is valid for what concerns the total number of protons above 2 MeV. Assuming a uniform angular distribution over $\pm 15°$, we retrieved a value of $\approx 3 \times 10^{11}$ of total protons, which is coherent with the scaling reported in [7]. While comprehensive details about the experimental campaign will be the topic of a dedicated article, this preliminary result demonstrates the effectiveness of the developed instrument for laser-driven proton spectroscopy.

V. Conclusion

The quantitative characterization of laser proton sources poses some challenges due to the specific properties of the involved physical process. In this work, we presented an active, real-time spectrometer based on a simple data analysis. The system is based on the magnetic dispersion of charged particles and can discriminate protons from heavy ions, thanks to a carefully designed differential filter. The spectrometer can provide the calibrated spectrum in the solid angle subtended by a pinhole, adopting silicon photodiode arrays. Each pixel is equipped with its readout electronics, appropriately selected considering the characteristics of the laser-driven spectrum.

The main components of the device were sized and characterized experimentally. The analytical model of the system was validated through Monte Carlo simulations, showing how the operating principle is effective, both in the discrimination of heavy ions from protons, and in the reconstruction of reference laser-driven exponential spectrum. The test performed during the campaign on the 1-PW laser VEGA-3 proved the effective implementation of the device in particle acceleration experiments and its spectroscopic capabilities.

The proposed instrument provides an alternative approach to measure laser-driven spectra, overcoming some limitations of conventional diagnostics, and paving the way for the exploitation of laser sources for their foreseen applications.

Acknowledgment

The authors thank the CLPU and its staff for the management of the experimental campaign and LaserLab Europe for its financial support for travel and accommodation.

References

[1] D. Strickland and G. Mourou, "Compression of amplified chirped optical pulses," *Opt. Commun.*, vol. 56, no. 3, pp. 219–221, Dec. 1985.
[2] P. Bolton, K. Parodi, and J. Schreiber, *Applications of Laser-Driven Particle Acceleration*. Boca Raton, FL, USA: CRC Press, 2018.
[3] M. Passoni, L. Fedeli, and F. Mirani, "Superintense laser-driven ion beam analysis," *Sci. Rep.*, vol. 9, no. 1, p. 9202, Jun. 2019.
[4] M. Passoni et al., "Advanced laser-driven ion sources and their applications in materials and nuclear science," *Plasma Phys. Controlled Fusion*, vol. 62, no. 1, Jan. 2020, Art. no. 014022.
[5] F. Mirani et al., "Integrated quantitative PIXE analysis and EDX spectroscopy using a laser-driven particle source," *Sci. Adv.*, vol. 7, no. 3, Jan. 2021, Art. no. eabc8660.
[6] F. Mirani, D. Calzolari, A. Formenti, and M. Passoni, "Superintense laser-driven photon activation analysis," *Commun. Phys.*, vol. 4, no. 1, p. 185, Aug. 2021.
[7] F. Mirani, A. Maffini, and M. Passoni, "Laser-driven neutron generation with near-critical targets and application to materials characterization," *Phys. Rev. Appl.*, vol. 19, no. 4, Apr. 2023, Art. no. 044020.
[8] A. Maffini, F. Mirani, A. C. Giovannelli, A. Formenti, and M. Passoni, "Laser-driven production with advanced targets of copper-64 for medical applications," *Frontiers Phys.*, vol. 11, Jul. 2023, Art. no. 1223023.
[9] Z. Sun, "Production of nuclear medicine radioisotopes with ultra-intense lasers," *AIP Adv.*, vol. 11, no. 4, Apr. 2021, Art. no. 040701.
[10] A. Macchi, M. Borghesi, and M. Passoni, "Ion acceleration by super-intense laser-plasma interaction," *Rev. Mod. Phys.*, vol. 85, no. 2, pp. 751–793, May 2013.
[11] H. Daido, M. Nishiuchi, and A. S. Pirozhkov, "Review of laser-driven ion sources and their applications," *Rep. Prog. Phys.*, vol. 75, no. 5, May 2012, Art. no. 056401.
[12] I. Prencipe et al., "Development of foam-based layered targets for laser-driven ion beam production," *Plasma Phys. Controlled Fusion*, vol. 58, no. 3, Mar. 2016, Art. no. 034019.
[13] A. Pazzaglia, L. Fedeli, A. Formenti, A. Maffini, and M. Passoni, "A theoretical model of laser-driven ion acceleration from near-critical double-layer targets," *Commun. Phys.*, vol. 3, no. 1, p. 133, Aug. 2020.
[14] L. Fedeli, A. Formenti, A. Pazzaglia, F. M. Arioli, A. Tentori, and M. Passoni, "Enhanced laser-driven hadron sources with nanostructured double-layer targets," *New J. Phys.*, vol. 22, no. 3, Mar. 2020, Art. no. 033045.
[15] P. Bradford et al., "EMP control and characterization on high-power laser systems," *High Power Laser Sci. Eng.*, vol. 6, p. e21, Jan. 2018.
[16] K. Nelissen et al., "Characterisation and modelling of ultrashort laser-driven electromagnetic pulses," *Sci. Rep.*, vol. 10, no. 1, p. 3108, Feb. 2020.
[17] P. R. Bolton et al., "Instrumentation for diagnostics and control of laser-accelerated proton (ion) beams," *Phys. Medica*, vol. 30, no. 3, pp. 255–270, May 2014.
[18] G. Milluzzo, G. Petringa, R. Catalano, and G. A. P. Cirrone, "Handling and dosimetry of laser-driven ion beams for applications," *Eur. Phys. J. Plus*, vol. 136, no. 11, p. 1170, Nov. 2021.
[19] F. Nürnberg et al., "Radiochromic film imaging spectroscopy of laser-accelerated proton beams," *Rev. Sci. Instrum.*, vol. 80, no. 3, pp. 1–14, Mar. 2009.
[20] M. J. Butson, P. K. Yu, T. Cheung, and P. Metcalfe, "Radiochromic film for medical radiation dosimetry," *Mater. Sci. Eng., R, Rep.*, vol. 41, pp. 61–120, Sep. 2003.

[21] V. Scuderi et al., "TOF diagnosis of laser accelerated, high-energy protons," *Nucl. Instrum. Methods Phys. Res. A, Accel. Spectrom. Detect. Assoc. Equip.*, vol. 978, Oct. 2020, Art. no. 164364.
[22] V. Scuderi et al., "Time of flight based diagnostics for high energy laser driven ion beams," *J. Instrum.*, vol. 12, no. 3, Mar. 2017, Art. no. C03086.
[23] S. Vallières et al., "Thomson parabola and time-of-flight detector cross-calibration methodology on the ALLS 100 TW laser-driven ion acceleration beamline," *Rev. Sci. Instrum.*, vol. 91, no. 10, pp. 1–11, Oct. 2020.
[24] K. Harres et al., "Development and calibration of a Thomson parabola with microchannel plate for the detection of laser-accelerated MeV ions," *Rev. Sci. Instrum.*, vol. 79, no. 9, pp. 1–9, Sep. 2008.
[25] R. Prasad et al., "Calibration of Thomson parabola—MCP assembly for multi-MeV ion spectroscopy," *Nucl. Instrum. Methods Phys. Res. A, Accel. Spectrom. Detect. Assoc. Equip.*, vol. 623, no. 2, pp. 712–715, Nov. 2010.
[26] A. McIlvenny et al., "Absolute calibration of microchannel plate detector for carbon ions up to 250 MeV," *J. Instrum.*, vol. 14, no. 4, Apr. 2019, Art. no. C04002.
[27] J. T. Gudmundsson, "Physics and technology of magnetron sputtering discharges," *Plasma Sources Sci. Technol.*, vol. 29, no. 11, Nov. 2020, Art. no. 113001.
[28] K. Sarakinos, J. Alami, and S. Konstantinidis, "High power pulsed magnetron sputtering: A review on scientific and engineering state of the art," *Surf. Coat. Technol.*, vol. 204, no. 11, pp. 1661–1684, Feb. 2010.
[29] S. Reinhardt, C. Granja, F. Krejci, and W. Assmann, "Test of pixel detectors for laser-driven accelerated particle beams," *J. Instrum.*, vol. 6, no. 12, Dec. 2011, Art. no. C12030.
[30] S. Reinhardt, W. Draxinger, J. Schreiber, and W. Assmann, "A pixel detector system for laser-accelerated ion detection," *J. Instrum.*, vol. 8, no. 3, Mar. 2013, Art. no. P03008.
[31] I. Prencipe et al., "Efficient laser-driven proton and bremsstrahlung generation from cluster-assembled foam targets," *New J. Phys.*, vol. 23, no. 9, Sep. 2021, Art. no. 093015.
[32] D. Jung et al., "Efficient carbon ion beam generation from laser-driven volume acceleration," *New J. Phys.*, vol. 15, no. 2, Feb. 2013, Art. no. 023007.
[33] J. F. Ziegler, M. D. Ziegler, and J. P. Biersack, "SRIM—The stopping and range of ions in matter," *Nucl. Instrum. Methods Phys. Res. B, Beam Interact. Mater. At.*, vol. 268, nos. 11–12, pp. 1818–1823, Jun. 2010.
[34] D. Dellasega, F. Mirani, D. Vavassori, C. Conti, and M. Passoni, "Role of energetic ions in the growth of fcc and ω phases in Ti films deposited by HiPIMS," *SSRN Electron. J.*, vol. 556, Aug. 2021, Art. no. 149678.
[35] D. Vavassori, F. Mirani, F. Gatti, D. Dellasega, and M. Passoni, "Role of magnetic field and bias configuration on HiPIMS deposition of W films," *Surf. Coat. Technol.*, vol. 458, Apr. 2023, Art. no. 129343.
[36] J. T. Gudmundsson, N. Brenning, D. Lundin, and U. Helmersson, "High power impulse magnetron sputtering discharge," *J. Vac. Sci. Technol. A, Vac., Surf., Films*, vol. 30, no. 3, May 2012.
[37] A. Maffini et al., "Towards compact laser-driven accelerators: Exploring the potential of advanced double-layer targets," *EPJ Techn. Instrum.*, vol. 10, no. 1, p. 15, Jun. 2023.
[38] V. M. Marx et al., "The influence of a brittle Cr interlayer on the deformation behavior of thin Cu films on flexible substrates: Experiment and model," *Acta Mater.*, vol. 89, pp. 278–289, May 2015.
[39] N. Ali, W. Ahmed, C. A. Rego, and Q. H. Fan, "Chromium interlayers as a tool for enhancing diamond adhesion on copper," *Diamond Rel. Mater.*, vol. 9, no. 8, pp. 1464–1470, Aug. 2000.
[40] M. Esposito, T. Price, T. Anaxagoras, and N. M. Allinson, "Geant4-based simulations of charge collection in CMOS active pixel sensors," *J. Instrum.*, vol. 12, no. 3, Mar. 2017, Art. no. P03028.
[41] S. Meroli, D. Passeri, and L. Servoli, "Measurement of charge collection efficiency profiles of CMOS active pixel sensors," *J. Instrum.*, vol. 7, no. 9, Sep. 2012, Art. no. P09011.
[42] D. A. Neamen and D. Biswas, *Semiconductor Physics and Devices*. New York, NY, USA: McGraw-Hill, 2011.
[43] J. Allison et al., "Recent developments in GEANT4," *Nucl. Instrum. Methods Phys. Res. A, Accel., Spectrometers, Detect. Assoc. Equip.*, vol. 835, pp. 186–225, Nov. 2016.
[44] A. Alejo et al., "Recent developments in the Thomson parabola spectrometer diagnostic for laser-driven multi-species ion sources," *J. Instrum.*, vol. 11, no. 10, Oct. 2016, Art. no. C10005.
[45] C. Salgado-López et al., "Angular-resolved Thomson parabola spectrometer for laser-driven ion accelerators," *Sensors*, vol. 22, no. 9, p. 3239, Apr. 2022.
[46] M. Ehret et al., "Stability and debris-mitigation of a solid tape target delivery system for intense laser-matter interactions towards high-repetition-rate," *Plasma Phys. Controlled Fusion*, vol. 66, no. 4, Apr. 2024, Art. no. 045003. [Online]. Available: http://iopscience.iop.org/article/10.1088/1361-6587/ad2690
[47] W. Seibt, K. E. Sundström, and P. A. Tove, "Charge collection in silicon detectors for strongly ionizing particles," *Nucl. Instrum. Methods*, vol. 113, no. 3, pp. 317–324, Dec. 1973.
[48] R. N. Williams and E. M. Lawson, "The plasma effect in silicon semiconductor radiation detectors," *Nucl. Instrum. Methods*, vol. 120, no. 2, pp. 261–268, Sep. 1974.
[49] M. Zimmer et al., "Analysis of laser-proton acceleration experiments for development of empirical scaling laws," *Phys. Rev. E, Stat. Phys. Plasmas Fluids Relat. Interdiscip. Top.*, vol. 104, no. 4, Oct. 2021, Art. no. 045210.

Francesco Gatti received the M.Sc. degree in nuclear engineering from Politecnico di Milano, Milan, Italy, in 2021, where he is currently pursuing the Ph.D. degree.

His research interests include laser–plasma acceleration targeting and diagnostics.

Francesco Mirani received the M.Sc. degree in nuclear engineering and the Ph.D. degree from the Politecnico di Milano, Milan, Italy, 2017 and 2021, respectively.

He is currently a Post-Doctoral Researcher at Politecnico di Milano. His research interests include laser-based PIXE.

Dario Rastelli received the M.Sc. degree in telecommunication engineering from Politecnico di Milano, Milan, Italy, in 2003.

He is the Co-Founder and the Technical Manager of RAYLAB S.r.l., Bergamo, Spain, a company developing innovative radiation detectors and monitors.

Davide Mazzucconi received the Ph.D. degree in energy and nuclear science and technology from Politecnico di Milano, Milan, Italy, in 2020.

He is a Researcher in the field of Nuclear Measurements and Instrumentation at the Department of Energy, Politecnico di Milano, and a Nuclear Engineer. His research activity is related to numerical and experimental radiation detection and dosimetry, radiation therapy, hadrontherapy, gas, and solid-state micro–nanodosimetry.

José Luis Henares received the M.Sc. degree in laser physics and technology from the University of Salamanca, Salamanca, Spain, in 2011, and the Ph.D. degree from GANIL, Caen, France, in 2016.

He is working on condensable ion production by resonant laser ionization. He is currently a Specialized Scientist at Centro de Láseres Pulsados (CLPU), Salamanca, Spain. His domains of expertise are high-power laser experiments and laser-driven ion source development.

Antonia Morabito received the master's degree in nuclear and subnuclear physics from the University of Calabria, Rende, Italy, in 2011, and the Ph.D. degree in accelerator physics from the Sapienza University of Rome, Rome, Italy, in 2021, with ELI-ALPS support.

After that, she started to work as an early-stage researcher at Extreme Light Infrastructure Attosecond Laser Plasma Source (ELI-ALPS), Szeged, Hungary, in February 2015. She is currently a Postdoctoral Researcher within the frame of the ELI-ERIC IMPULSE project at Centro de Laseres Pulsados (CLPU), Salamanca, Spain. Her thesis focuses on the transport and manipulation of laser-driven proton beams for diagnostics and applications.

Andrea Pola received the M.Sc. degree in nuclear engineering and the Ph.D. degree from Politecnico di Milano, Milan, Italy, in 2002 and 2006, respectively.

He is working on semiconductor detectors for neutron spectrometry and microdosimetry. He is currently a Full Professor of "Nuclear Measurements and Instrumentation" at Politecnico di Milano. His main scientific interests are dosimetry, microdosimetry, nanodosimetry, and spectrometry of complex radiation fields.

Matteo Passoni received the M.Sc. degree in nuclear engineering and the Ph.D. degree from the Politecnico di Milano, Milan, Italy, in 2000 and 2004, respectively.

He is currently a Full Professor in physics of matter at Politecnico di Milano. His main scientific interests are laser-plasma interaction and laser–plasma-based particle acceleration, plasma physics, and materials for nuclear fusion.

Open Access funding provided by 'Politecnico di Milano' within the CRUI CARE Agreement